Catalytic Conversion of Furans to Aromatics over Ga-MFI Zeotypes with Varying Gallium Content

I&EC research
Industrial & Engineering Chemistry Research

pubs.acs.org/IECR
Article

Catalytic Conversion of Furans to Aromatics over Ga-MFI Zeotypes with Varying Gallium Content

Guido J. L. de Reijer,* Andreas Schaefer, Anders Hellman, and Per-Anders Carlsson*

Cite This: *Ind. Eng. Chem. Res.* 2025, 64, 2025−2035
Read Online

ABSTRACT: To address the need for a sustainable chemical industry, commodity chemicals including the aromatics benzene, toluene, and xylenes (BTX) must be produced from renewable feedstocks such as biomass-derived furans. Here, the conversion of 2,5-dimethylfuran (2,5-dmf) into aromatics was studied by step-response experiments in a chemical flow reactor, catalyzed by a series of phase-pure MFI framework Ga-zeotype catalysts with a gallium content ranging from 0.5 to 11 wt %. The lifetime of the catalyst and its aromatic production increase with increasing gallium content, demonstrating a near-40-fold increase in benzene production when increasing the gallium content from 0.5 to 8.6 wt %, while a further increase to 11 wt % leads to a decrease in benzene production due to rapid deactivation of the catalyst by coke. Acid site analysis reveals that aromatization occurs on strong Brønsted acid sites, promoted by strong Lewis acid sites, while isomerization occurs on weak Brønsted acid sites. At high gallium content (≥6.0 wt %), gallium-based nanoparticles are formed, whose presence results in faster catalyst deactivation. The catalysts were active for five consecutive cycles and were readily regenerated, recovering the majority of their initial acid sites.

INTRODUCTION

The growing demand for a sustainable chemical industry motivates the search for alternatives to petroleum-based feedstocks. Chemicals that are interesting for this transition are the light monocyclic aromatics benzene, toluene, and xylenes (BTX), used in the production of dyes, pharmaceuticals, pesticides, plastics, pigments, and solvents.[1] While the demand for benzene in the leading industrial countries is projected to remain stable up to 2040, its demand in the rest of the world will skyrocket from 300 million tonnes in 2020 up to 800 million tonnes in 2040.[2] Traditionally, BTX is produced via the catalytic reforming of naphtha, although processes have recently been developed to produce them from a renewable and potentially sustainable feedstock: lignocellulosic biomass. In countries with a developed forest industry, such as Sweden, domestic BTX needs may be fully covered by biomass feedstocks, provided there is a suitable chemical process. Lignocellulosic biomass can be converted into molecules such as the furanics furfural, 5-hydroxymethylfurfural, 2,5-dicarboxylic acid, and 2,5-dmf, through processes based on gasification, pyrolysis, and catalytic fast pyrolysis.[3−6] These molecules can be used directly as fuel[7−11] or as platform chemicals for further conversion into BTX.[12−16]

Suitable catalysts for these reactions are microporous acidic zeolites, possessing high thermal stability, high surface area, shape-selectivity, and tunability. To illustrate, 2,5-dmf has been converted into para-xylene over zeolites via a Diels−Alder cycloaddition mechanism, using ethene as coreagent.[17−21] Several medium pore size frameworks, such as the MFI framework, are often employed as their pore size of roughly 5.5 Å[22] matches the molecular dimensions of monocyclic aromatics (5.1−5.7 Å)[23] and thus aids the formation of BTX. In addition, BTX formation has been increased by introducing metals into the zeolite, such as Zn[24−27] and Ga.[20,25−30] Through ion exchange or impregnation, the metals end up as extra-framework species such as oxides (GaO^+/Ga_2O_3), increasing BTX selectivity by inter alia narrowing the micropores.[28] Moreover, extra-framework species are often associated with strong Lewis acid sites (LAS), which can display synergistic interactions with Brønsted acid sites (BAS) formed by framework aluminum or gallium.[31] In this case, the extra-framework species are referred to as framework-associated gallium and their presence is often paired to a decrease in the BAS/LAS ratio.[25,32]

In our recent work, the performance of an MFI framework zeotype was studied with isomorphously substituted gallium instead of aluminum.[30] When comparing the Ga-MFI catalyst to aluminum-containing ZSM-5 zeolites of similar or higher

Received: September 12, 2024
Revised: January 8, 2025
Accepted: January 14, 2025
Published: January 21, 2025

https://doi.org/10.1021/acs.iecr.4c03465
Ind. Eng. Chem. Res. 2025, 64, 2025−2035

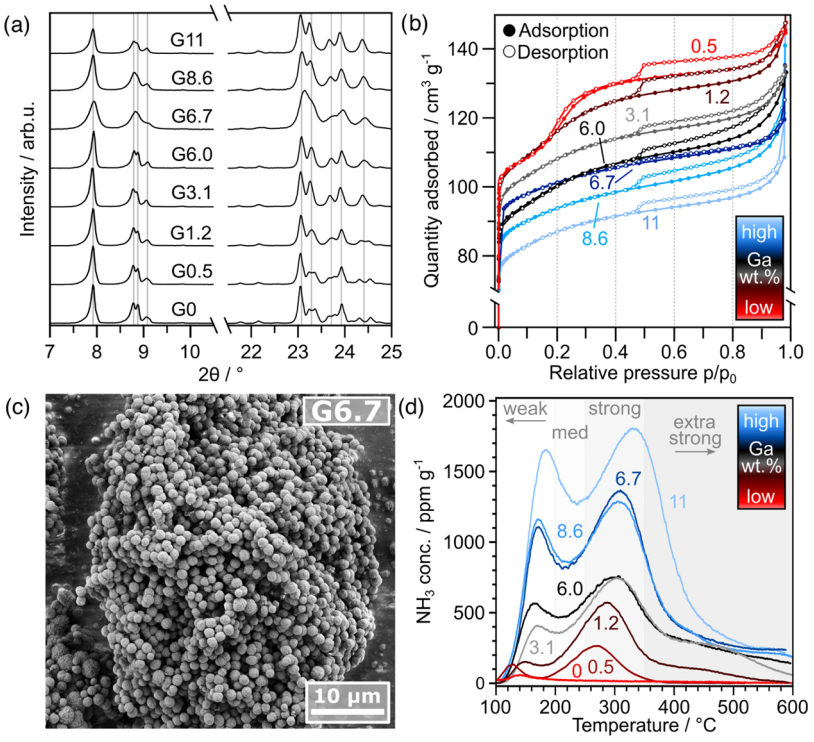

Figure 1. Overview of the structural analysis including a close-up of the XRD diffractograms (a) where the gray lines indicate the MFI-structure,[41] nitrogen physisorption (b) where the numbers denote the gallium content in wt %, a representative SEM image of zeotype G6.7 (c), and the NH_3-TPD profiles (d).

acidity, it displayed an increased conversion and selectivity toward BTX in both cases, in particular toward benzene with a near 10-fold increase. Additionally, the lifetime of the catalyst was extended which was likely caused by the lower strength of the gallium BAS compared to the aluminum BAS, slowing down coke formation.[33] The increased performance of Ga-MFI zeotypes in the conversion of 2,5-dmf toward BTX motivates further studies in which key performance parameters, such as the gallium content, are systematically varied.

Here, MFI framework zeotypes with different Ga contents were synthesized using a bottom-up hydrothermal synthesis that was optimized to ensure phase-purity of catalysts with gallium contents up to 11 wt %, either by using different templates or by increasing the duration of the crystallization step. The effect of gallium on the structural and chemical characteristics of the catalyst was analyzed by several techniques, as described in the experimental section. The catalytic performance was studied during multiple consecutive cycles of reaction, separated by regeneration steps.

■ EXPERIMENTAL SECTION

The materials studied in this work are gallium zeotypes comprising the MFI framework, synthesized via hydrothermal crystallization based on a method described elsewhere.[30] Full details of the synthesis can be found in the Supporting Information (SI). Purely siliceous MFI zeolite (silicalite-1) was used for comparison, named G0 which indicates a Ga content of 0 wt %.[34]

The elemental composition of the catalysts, for elements with an atomic number larger than eight, was determined by X-ray fluorescence spectroscopy (XRF) using an AXIOS spectrometer (Malvern-Panalytical) assuming silicon and gallium to be in their oxide form.

The crystallinity of the catalysts was measured by powder X-ray diffraction (XRD) on a Bruker AXS D8 Discover diffractometer with monochromatic Cu−Kα radiation (1.5406 Å) from 5 to 50° 2θ.

Thermogravimetric analysis (TGA) coupled with differential scanning calorimetry (DSC) was carried out from 30 to 900 °C in 60 mL/min airflow using a Mettler Toledo TGA/DSC 3+ STARe system.

Textural properties of the catalysts were determined using N_2-physisorption at 77 K on a Micromeritics Tristar 3000 instrument after a pretreatment of 16 h in N_2 at 250 °C. Apparent surface areas were determined using the BET method[35] in the relative pressure range of p/p_0 = 0.002−0.03, according to the consistency criteria.[36] The microporous volume was determined by the t-plot method with the Harkins and Jura equation,[37] using a thickness of t = 5.0−8.0 Å to minimize the underestimation caused by the curvature effect.[38]

Morphological analysis was performed using scanning electron microscopy (SEM) on a Zeiss Ultra 55 FEG SEM (1.5 kV), using energy-dispersive X-ray spectroscopy (EDX) on a FEI Quanta 200 FEG ESEM (20 kV), and using high-angle annular dark field scanning transmission electron microscopy (HAADF-STEM) on a FEI Titan 80-300 TEM (300 kV). Powder samples were loaded on carbon tape stuck to an Al holder (SEM/EDX), uncoated or coated with 4 nm Au using a Leica EM ACE600 sputter coater, as well as dispersed on Holey Carbon Film supported Cu grids (HAADF-STEM, Ted Pella).

Acid sites were analyzed by temperature-programmed desorption of ammonia (NH_3-TPD) in the catalytic reactor right before and directly after the catalytic tests, as well as after an oxidative calcination step after the reaction and after five cycles. Full details can be found in the SI.

https://doi.org/10.1021/acs.iecr.4c03465
Ind. Eng. Chem. Res. 2025, 64, 2025−2035

Table 1. Physicochemical Properties and Catalytic Performance of the Synthesized Ga-MFI Zeotypes

sample	SA[a] $m^2\ g^{-1}$	V_{micro}[b] $cm^3\ g^{-1}$	acidity[c] mmol g^{-1}	BAS/LAS[d]	benz. one h[e] mmol g^{-1}	benz. three h[e] mmol g^{-1}	S_{coke}[f] %
G0	395	0.175	0.002	∞	0.00	0.00	0.0
G0.5	445	0.185	0.039	∞	0.05	N/A	4.2
G1.2	435	0.175	0.119	3.3	0.39	N/A	7.7
G3.1	420	0.162	0.268	3.0	0.53	0.89	8.0
G6.0	390	0.142	0.256	1.3	0.65	0.73	10.6
G6.7	401	0.148	0.423	2.1	1.39	1.65	12.7
G8.6	368	0.135	0.433	1.8	1.28	1.89	14.3
G11	336	0.127	0.612	3.8	0.99	1.14	16.4

[a]Apparent surface area determined by N_2-physisorption and BET method[35] (p/p_0= 0.002 − 0.03 following consistency criteria[36]). [b]By t-plot method[37] (Harkins and Jura equation, t= 5.0 − 8.0 Å). [c]Acid site density from NH_3-TPD. [d]Ratio of Brønsted to Lewis acid sites from pyridine-FTIR. [e]Benzene produced after 1 or 3 h 2,5-dmf conversion at 500 °C. [f]Total coke selectivity after 1 h (G0.5 and G1.2) or 3 h 2,5-dmf conversion at 500 °C.

Additional acid site analysis was performed with pyridine adsorption experiments using diffuse reflectance infrared Fourier transform spectroscopy (DRIFTS) on a BRUKER VERTEX 70 spectrometer after adsorption at 150 and 300 °C, to probe either all acid sites or only the strong acid sites, respectively. Full details can be found in the SI (Figure S1).

Evaluation of the catalytic activity and selectivity of the zeotypes was carried out using a fixed-bed reactor. The liquid reactant 2,5-dmf was introduced in the reactor through a gas saturator (ca. 720 ppm, WHSV = 0.66 ± 0.04 $g_{dmf}\ g_{cat}^{-1}h^{-1}$) and the reaction was performed at 500 °C for 1 or 3 h.

The effluent product mixture was analyzed online by ion−molecule-reaction mass spectrometry (IMR-MS) on an Airsense Compact (V&F) and by Fourier-transform infrared spectroscopy (FTIR) on a gas analyzer (MKS MultiGas 2030). Products were quantified with the MKS software suite MG2000 v.10.2 and FTIR-library v.R3 by FTIR according to a method described in previous works,[39,40] complemented by IMR-MS. Full details can be found in Table S2 in the SI.

For selected zeotypes, the stability of the catalysts was investigated by subjecting them to a total of five cycles of 3 h 2,5-dmf conversion at 500 °C, separated by 90 min oxidative regeneration in 20% O_2 at 600 °C (5 °C/min).

RESULTS AND DISCUSSION

This section describes the characterization of the physicochemical properties of the synthesized catalysts followed by the analysis of their catalytic performance in the conversion of 2,5-dmf.

Catalyst Characterization. The elemental composition of the catalysts obtained by XRF spectroscopy is shown in Table S3 in the SI. Besides the main elements silicon, gallium, and oxygen, some samples contain low levels of impurities such as sodium or potassium. The former originates from the precursor sodium hydroxide whereas the latter comes from a KOH bath used to clean the Teflon liners used for synthesis.

X-ray diffraction was measured to identify the crystalline phases and a close-up of the diffractograms is shown in Figure 1a. The full diffractograms are shown in Figure S2 in the SI. All measured peaks are associated with crystal lattice planes that are characteristic of the MFI framework structure, of which the most intense are marked with vertical gray lines.[41] The absence of other peaks indicates that no other crystalline phases of long-range order have formed. Variations in the peak size and shape such as peak broadening and overlap are observed when the Ga content is increased, indicating the presence of lattice distortions caused by defects.[42] This effect of the large Ga atom on the lattice crystallinity[43] is illustrated by the merging of the peaks at 23.2 and 23.4°, visible in G0 and G0.5, into one peak at 23.3° as well as the merging of the peaks at 24.4 and 24.6°. Besides defects, the broad peaks in zeotype G6.7 could indicate a smaller crystallite size.

Additionally, the effect of gallium was shown by the incomplete crystallization of a high gallium precursor gel (Si/Ga = 10) into the MFI structure. After 5 days of crystallization, the synthesized catalyst G7.8-amorph contains an amorphous phase, as indicated by a broad peak from 20 to 25° in the XRD diffractogram (Figure S3 in the SI). To prevent this and ensure the complete crystallization of gels with a high gallium content to the MFI phase, the duration of the crystallization was increased from 5 to 10 days, resulting in G6.0, G12-imp, and G14-imp. Here, "imp" denotes the presence of phase impurities detected besides MFI, such as α-quartz[44] (SiO_2) and gallium albite[45] ($GaNaSi_3O_8$), as shown in Figure S3b in the SI. These phases were formed because of the long crystallization time and the high sodium content of the precursor gel. NaOH was added to neutralize the acidic Ga precursor and to increase the pH of the synthesis gel to the basic conditions required for zeotype crystallization. All three zeotypes G7.8-amorph, G12-imp, and G14-imp possess a low apparent surface area, low number of acid sites, and exhibit a low conversion of 2,5-dmf (Table S4 in the SI). For the synthesis of G6.0, less sodium hydroxide was needed and phase-pure MFI zeotype was obtained, as shown in Figures 1 and S2 in the SI. These issues were solved by using the basic template TPAOH instead of TPABr and reducing the duration of the crystallization step to 5 days again. This resulted in the synthesis of phase-pure MFI framework zeotypes with a high gallium content, named G6.7, G8.6, and G11.

The textural properties of the catalysts were studied by N_2-physisorption and the isotherms are shown in Figure 1b. An increase in gallium content appears to result in a decrease in the total nitrogen uptake, as G0.5 (red) shows the highest uptake and G11 (light blue) the lowest.

All zeotypes display a steep uptake of nitrogen at low relative pressures (p/p_0< 0.01), associated with the filling of micropores.[46] The amount of nitrogen adsorbed in the micropores in this initial step decreases stepwise with increasing gallium content, demonstrating a decrease in microporous volume. The isotherms are composites of type I, associated with microporous adsorbents, and type IV, associated with mesoporous adsorbents. All isotherms display hysteresis

https://doi.org/10.1021/acs.iecr.4c03465
Ind. Eng. Chem. Res. 2025, 64, 2025−2035

loops of type H4 from p/p_0= 0.42 − 0.98, caused by capillary condensation in mesopores. These mesopores are thought to be between crystallites or in larger aggregates of zeotype crystals.[46] The sharp cutoff in the hysteresis at p/p_0 = 0.42 could be used to determine the pore size distribution but is rather regarded as an artifact, typically observed for N_2 adsorption at 77 K. This artifact, named the tensile strength effect, is caused by the mechanical stability of liquid nitrogen in micropores.[47,48] The adsorption isotherm of G0.5, as well as G0 in Figure S4 in the SI, displays a second step between p/p_0= 0.1 − 0.25, accompanied by a slight hysteresis. Low-pressure hysteresis could indicate insufficient outgassing prior to adsorption or improper equilibration during the measurement.[49] Instead, this step is considered to be caused by noninert N_2-molecules that undergo reorientation to permit a more favorable quadrupole−quadrupole interaction. First, at low pressures, the adsorbed nitrogen transitions from a disordered phase, presumably a fluid, to a localized fluid-like phase. Second, a quasi-crystalline order is formed by the formation of a chain-like solid phase, displaying a second adsorption step, which is accompanied by hysteresis to overcome the energy barrier associated with the reverse reorientation of the adsorbed nitrogen.[50−53] For zeotypes with a gallium content of ≥1.2 wt %, the hysteresis loop is not observed due to preferential adsorption of nitrogen to gallium, essentially skipping the initial disordered phase while the second transition is smoothed out.[54]

An increase in gallium content is paralleled by a reduction in the available surface area and microporous volume, as shown in Table 1. For example, the apparent surface area decreases from 445 $m^2\ g^{-1}$ down to 336 $m^2\ g^{-1}$ when increasing the Ga content (samples G0.5 to G11). Similarly, the microporous volume decreases from 0.185 $cm^3\ g^{-1}$ in G0.5 to 0.127 $cm^3\ g^{-1}$ in G11. Care must be taken in interpreting these values as measures of absolute volume because helium was used to measure the free space before nitrogen adsorption. Helium may get trapped inside micropores, which renders them inaccessible to nitrogen, resulting in an underestimation of the true microporous volume. The observed inverse correlation between both the surface area and the microporous volume with changing gallium content can be explained by two reasons: first, the ionic radius of the substituting ion, gallium(III), is much larger than the radius of silicon(IV): 62 and 40 pm, respectively. Second, gallium can also be present inside the micropores, either as extra-framework species or as framework-associated species which is gallium positioned in the cation position in the proximity of framework gallium.[31] This effectively reduces the accessible space and surface area of the catalyst. The zeotype G6.0 has a lower surface area and microporous volume than the observed trend would suggest, likely owing to the longer crystallization time of 10 days instead of 5 days, favoring the formation of larger particles.

The morphological features of zeotypes were observed by SEM and an example of a recorded image of G6.7 is shown in Figure 1c (SEM images of other zeotypes are shown in Figure S5 in the SI). Here, G0 possesses the well-known' coffin-shape of two parallelepipeds embedded in one another whereas after gallium introduction in G0.5, G1.2, and G3.1, smaller, cubic-shaped crystals are formed. These crystals aggregate to form larger intergrown particles of various dimensions. When the duration of the crystallization is increased from five to 10 days, for G6.0, the crystal shape becomes more irregular and no microscopic order is visible. The zeotypes G6.7, G8.6, and G11 contain intergrowths of well-defined crystallites of different shapes and sizes, including the coffin-shaped. The individual spherical crystals in G6.7 are the smallest, typically ranging from 500 nm to 1 μm in diameter, which explains the peak broadening observed in the X-ray diffractogram in Figure 1a. The small crystal size could be beneficial to its catalytic performance because of the reduced lengths of diffusion pathways of reagents and products.

Further investigation of the morphology was performed by HAADF-STEM, as shown in Figure S6 in the SI. The G0 crystals, whose thickness makes them challenging to image at high magnification, are uniform in size and shape. All samples with a high gallium content of 6.0 wt % and higher contain nanoparticles, likely gallium oxide (GaO_x), indicated by bright, intense spots. Although not enough particles were imaged to give a statistical approximation, it appears that the number of nanoparticles increases in the order of G6.7 < G8.6 < G6.0 < G11. Additionally, the size of the nanoparticles also seems to follow this trend. These images confirm the presence of extra-framework gallium and explain why a decrease in SSA and microporous volume is observed when the Ga content is increased: the large nanoparticles have a low surface area compared to micropores and potentially block access to the micropores. Moreover, the relatively high number of gallium oxide nanoparticles in G6.0 validates the suggestion that the increased crystallization time resulted in sintering and formation of extra Ga-based nanoparticles.

To determine the distribution of the different elements throughout the crystals, EDX was measured, and the elemental maps of zeotype G8.6 are shown as an example in Figure S7 in the SI. The main components silicon, oxygen, and gallium are all homogeneously distributed over the different crystals, as well as the impurity potassium which was measured in low amounts. The presence or composition of the nanoparticles was not detectable at the micrometer length scale.

The hydrothermal stability of the final protic zeotypes was tested by TGA, as shown in Figure S8a in the SI. Here, all catalysts are stable over the temperature range of 30 to 900 °C, losing 1.4 wt % for G0 up to 3.1 wt % for G11. Most of the weight loss occurred between 100 and 200 °C, which is ascribed to the desorption of water that had been adsorbed from the air. However, a small second weight loss step can be seen for G11 (black) at 550 °C which is ascribed to the loss of NH_3, replacing the framework-attached NH_4 by H. This indicates that the calcination of the ion exchanged NH_4-G11 was incomplete, possibly due to a low presence of oxygen in a muffle furnace with insufficient ventilation. Nevertheless, its catalytic performance was not affected because of the pretreatment step before the reaction (1 h in 20% oxygen at 500 °C), ensuring full conversion of NH_4-G11 to H-G11. An increase in gallium content appears to correlate to an increase in water content, likely owing to the preferential adsorption of water to gallium and the acid sites it provides. To simulate the calcination of the zeotypes, TGA/DSC analysis was performed in airflow on the as-synthesized zeotypes (Figure S8b,c), still containing tetrapropylammonium (TPA). Here, all zeotypes display a large loss of weight between 380 and 500 °C, ascribed to the exothermic decomposition of TPA. The size of this weight loss decreases from 11 wt % in G0 (not shown) to 6.2 wt % in G11. This decrease in TPA content could be an indication that not all of the gallium atoms are isomorphously

https://doi.org/10.1021/acs.iecr.4c03465
Ind. Eng. Chem. Res. 2025, 64, 2025−2035

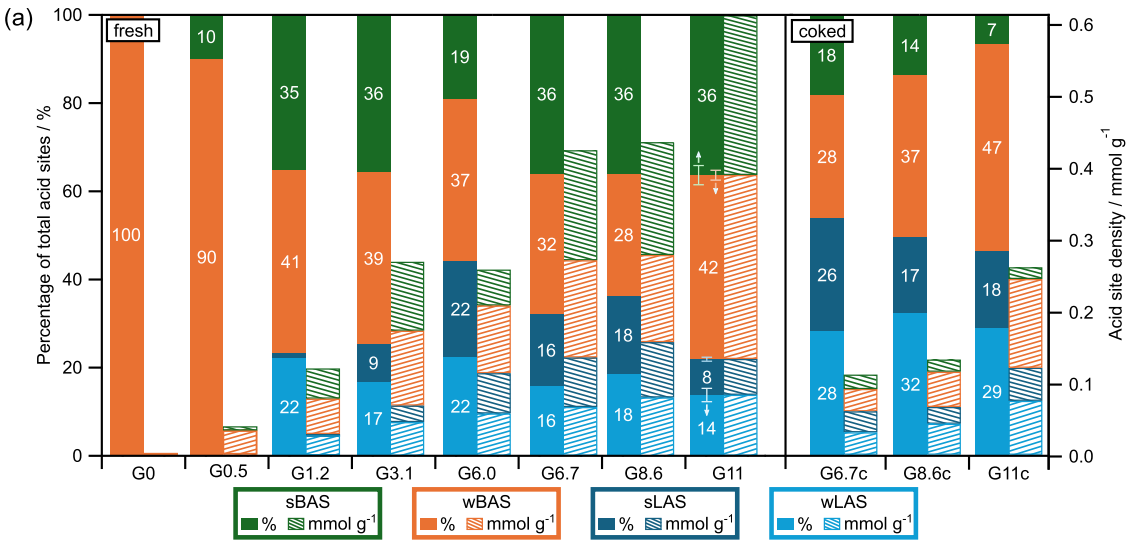

Figure 2. Distribution of the acid sites on the zeotypes as determined by pyridine adsorption given as a percentage (left axis) or as an acid site density based on NH_3-TPD (right axis). Sites are classified into strong and weak Brønsted acid sites (sBAS and wBAS), and strong and weak Lewis acid sites (sLAS and wLAS). G11 was measured twice and the error bars indicate the deviation from the average value. After exposure to 6 cycles of 3 h of 2,5-dmf conversion at 500 °C, pyridine adsorption was performed on the coked zeotypes G6.7c, G8.6c, and G11c.

substituted in the framework but instead present as extra-framework species, obstructing access for TPA.

The acidity of the Ga-zeotypes was measured by NH_3-TPD and the profiles are shown in Figure 1d. Purely siliceous MFI, G0 (bright red), contains almost no acid sites displaying only a minor peak around 140 °C ascribed to terminal silanol groups. After introducing gallium, two peaks appear, corresponding to a weak acid site below 200 °C and a strong acid site between 250 and 350 °C. Upon increasing the gallium content, both peaks increase in size which signifies an increase in the number of acid sites. Additionally, the peaks shift toward higher temperatures, indicating that each type of acid site becomes stronger, likely because of synergistic effects between multiple gallium species. This is further supported by an increase in the number of extra strong acid sites, desorbing NH_3 at temperatures >350 °C and mainly prevalent in G6.0, G6.7, G8.6, and G11. At 600 °C, ammonia was still desorbing from extra strong acid sites, suggesting that the TPD was incomplete. To limit structural damage to the catalysts, the temperature was not further increased but instead remained at 600 °C for 20 min to ensure complete desorption of NH_3 from the catalysts before the catalytic tests.

The TPD profiles were quantified and an overview of the acid site densities is shown in Tables 1 and S5 in the SI. Here, an increase in gallium content correlates to an increase in acid site density, ranging from 0.039 mmol g^{-1} for G0.5 to 0.612 mmol g^{-1} for G11. However, the series is not monotonically increasing as G6.0 has a relatively low acid site density of 0.256 mmol g^{-1}; close to G3.1 with an acid site density of 0.268 mmol g^{-1} even though it contains nearly twice the amount of gallium. Extending the crystallization duration from 5 days for G3.1 to 10 days for G6.0 has resulted in the sintering of gallium into extra-framework species, such as clusters or gallium-based nanoparticles, as was shown by HAADF-STEM.

Normalizing the number of acid sites to the gallium content reveals that each gallium atom in the high Ga content zeotypes, such as G6.0, G6.7, G8.6, G11, contributes less to forming an individual acid site, owing to the presence of extra-framework species such as nanoparticles.

To further elucidate the chemical environment of the acid sites, pyridine adsorption was studied by DRIFTS at different temperatures. Like ammonia, pyridine is a basic probe molecule that binds both to Brønsted acid sites, forming the pyridinium ion Py-H^+, and to Lewis acid sites. These different species absorb infrared light of different frequencies, allowing for the distinction between BAS and LAS. The background-subtracted FTIR spectra of the zeotypes after pyridine adsorption at 150 and 300 °C are shown in Figure S9 in the SI, focusing on the region of interest around the peaks ascribed to BAS (1545 cm^{-1}) and LAS (1455 cm^{-1}).[55] Adsorption at high temperature probes the strong and extra-strong acid sites while probing at low temperature probes all sites; the weak and medium strong acid sites are derived from the difference. An increase in gallium content corresponds to an increase in the number of BAS sites, in agreement with the results from NH_3-TPD. By contrast, the vibrations of the LAS (panel c and d) reveal a slightly different trend, with G6.0 having a relatively high number of LAS and G11 a relatively low number. After background subtraction, the peaks were integrated using the molar attenuation coefficients ϵ of ϵ_{BAS} = 1.67 and ϵ_{LAS} = 2.22.[56] The results are shown in Table 1 and Figure 2, displaying both the relative distribution of the different acid sites as well as the absolute density of each acid site based on NH_3-TPD.

G0 contains only weak Brønsted acid sites (wBAS), ascribed to terminal silanol groups. After introducing gallium, strong BAS (sBAS) are formed in G0.5, and a further increase to G1.2 also introduces weak Lewis acid sites (wLAS). Strong LAS (sLAS) are first detected in G3.1 although the majority of its sites are weak and strong BAS, with a BAS/LAS ratio of 3.0. This ratio shifts to 1.3 for G6.0 due to its high amount of sLAS and low amount of sBAS. G6.7 and G8.6 have similar acid site distributions while G11 has a notable high BAS/LAS ratio of 3.8, equaling a LAS content of 22%. As shown by HAADF-STEM, Ga-based nanoparticles are prevalent in the high Ga content zeotypes in varying degrees. However, this does not correlate to a specific detected acid site such as a Lewis acid site, since G11 contains more nanoparticles than G8.6 but has

https://doi.org/10.1021/acs.iecr.4c03465
Ind. Eng. Chem. Res. 2025, 64, 2025−2035

fewer Lewis acid sites. Therefore, the nanoparticles are suspected to not contribute to the formation of extra acid sites, although their presence might affect the strength and access of nearby sites. Pyridine FTIR shows that the strong and extra-strong sites can not simply be ascribed to one type of acid site, but are instead a combination of BAS and LAS; the latter potentially being present in complex ways as framework, framework-associated, or extra-framework species, analogous to what has been seen for Al-zeolites.[57]

Catalytic Activity and Selectivity. The catalytic performance was tested in a fixed-bed reactor by introducing 720 ppm 2,5-dmf at 500 °C and running the reaction for 1 or 3 h. The conversion and product selectivities (excluding coke) were calculated (see eqs 1 and 2 in the SI) and an overview of the main products over zeotype G6.7 is shown in Figure 3. At the start of the reaction, full conversion of 2,5-dmf into benzene takes place with a maximum selectivity of 95%. Toluene is also formed in low concentrations with a maximum selectivity of 6%, as well as alkenes such as ethene and propene. Xylenes were formed in very low concentrations and were only detected by MS, as shown in Figure S10 in the SI. After roughly 1.5 h time on stream (TOS), the conversion of 2,5-dmf and the benzene selectivity rapidly decrease to 53 and 10%, respectively, indicating deactivation of the catalyst toward aromatics. Simultaneously, the selectivity shifts to isomerization products including 2-methylcyclopentenone (2-mcpo), 3-methylcyclopentenone (3-mcpo), and 2,4-dimethylfuran (2,4-dmf), reaching 10, 6, and 63% selectivity after 3 h TOS at 14% conversion, respectively. In previous work, it was concluded that the isomerization toward 2,4-dmf is promoted by the steric confinement of the MFI framework, the presence of an acid site, and lower reaction temperatures of around 350 °C.[58] Moreover, the demethylation product 2-methylfuran (2-mf) is observed as well as the polycyclic aromatic indene; the latter peaking at 15% selectivity after 1 h TOS.

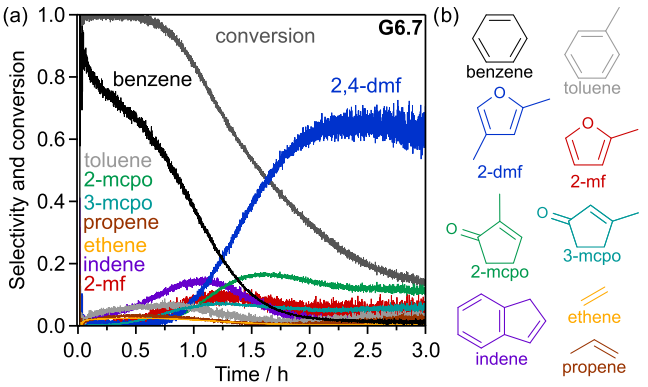

Figure 3. Conversion of 2,5-dmf and selectivities (a) of the main products including benzene, toluene, propene, ethene, 2-mcpo, 3-mcpo, 2,4-dmf, 2-mf, and indene (b) as a function of time over zeotype G6.7 for 3 h at 500 °C. Concentrations were determined every 2 s and the selectivities do not account for the formation of coke.

The conversion of 2,5-dmf was also performed under identical conditions for the other zeotypes, as shown in Figure 4. G0 was not active for the reaction (not shown), indicating that the presence of gallium and acid sites are required to convert 2,5-dmf.[30] G0.5 (a) displays a stable conversion of 72% to the isomerization products 2,4-dmf and 2-mcpo, with benzene only being detected during the initial minutes of the reaction. Linking selectivity with the acid site distributions (Figure 2), it follows that the weak Brønsted acid sites (wBAS) are responsible for the isomerization reactions while the sBAS are responsible for the production of monocyclic aromatics such as benzene, as well as polycyclic aromatics (indene), leading to further coking and deactivation of the few available sBAS. When the gallium content (and the number of sBAS) is increased, benzene becomes the main product at the start of the reaction, reaching 50% selectivity at 78% conversion over G1.2 (d). Even though the number of wBAS did not increase from G0.5 to G1.2, the production of 2-mcpo is higher after 1 h TOS with 23% selectivity at 55% conversion. Based on the decrease in benzene selectivity, it is assumed that the sBAS are deactivated. Logically, it follows that the increased 2-mcpo production is promoted by the wLAS present in G1.2. A further increase in the gallium content results in an initial benzene selectivity and conversion of 72 and 95% over G3.1 (b), respectively, while reaching 100% for G6.0 (e), G8.6 (c), and G11 (f). Even though G6.0 has more gallium than G3.1, it has fewer acid sites (0.256 vs 0.268 mmol g^{-1}), as well as fewer sBAS. This results in a faster deactivation toward benzene over G6.0 than over G3.1, reaching 12 and 28% selectivity after 0.75 h, respectively. The increased coking of G6.0 is illustrated by a high indene selectivity of 16% after 0.4 h. However, the initial benzene production over G6.0 is substantially higher, indicating that the other acid sites such as sLAS, promote benzene production. Like G6.7, all zeotypes demonstrate deactivation toward benzene accompanied by a shift in selectivity toward 2,4-dmf, although their lifetime varies. G8.6 displays the longest lifetime toward benzene production while G11, the zeotype with both the highest gallium content and the highest acid site density, deactivates toward benzene around 1.1 h. An explanation for this behavior is that the density of the strong Brønsted acid sites is too high, promoting the formation of coke via alkylation, condensation, and dehydrogenation.[59] Similar behavior was observed for aluminum-containing MFI-framework zeolites in another work, where the zeolite with an Al content of 3.5 wt % (0.538 mmol g^{-1} acid sites) deactivated twice as fast as a zeolite with an Al content of 1 wt % (0.173 mmol g^{-1} acid sites).[30]

The benzene concentrations measured during the first hour of the reaction are displayed in figure S11 in the SI. Here, a clear correlation is observed between the gallium content and benzene production: increasing the Ga content from 0 to 6.7 wt % increases the benzene production. Further increasing the gallium content to 8.6 and 11 wt % does not give a higher benzene yield, although these catalysts have a higher acid site density. One possible reason could be the smaller average crystal size of G6.7, promoting diffusion and mass transfer of reagents and products. However, after 0.7 h, the benzene production over G8.6 surpasses G6.7 as G8.6 appears to deactivate slower. The total production of benzene is quantified and shown in Tables 1 and S6 in the SI. Although more benzene is produced after 1 h TOS over G6.7 (1.39 mmol g^{-1}) than over G8.6 (1.28 mmol g^{-1}), this shifts to G8.6 (1.89 mmol g^{-1}) after 3 h TOS compared to 1.65 mmol g^{-1} over G6.7. As their acid site density and distribution is nearly identical, the presence of extra gallium in G8.6 appears to promote benzene production; potentially by providing extra-strong framework-associated acid sites. The effect of the smaller crystal size of G6.7 could be two-sided, as this also increases its surface-to-volume ratio, resulting in the

https://doi.org/10.1021/acs.iecr.4c03465
Ind. Eng. Chem. Res. 2025, 64, 2025−2035

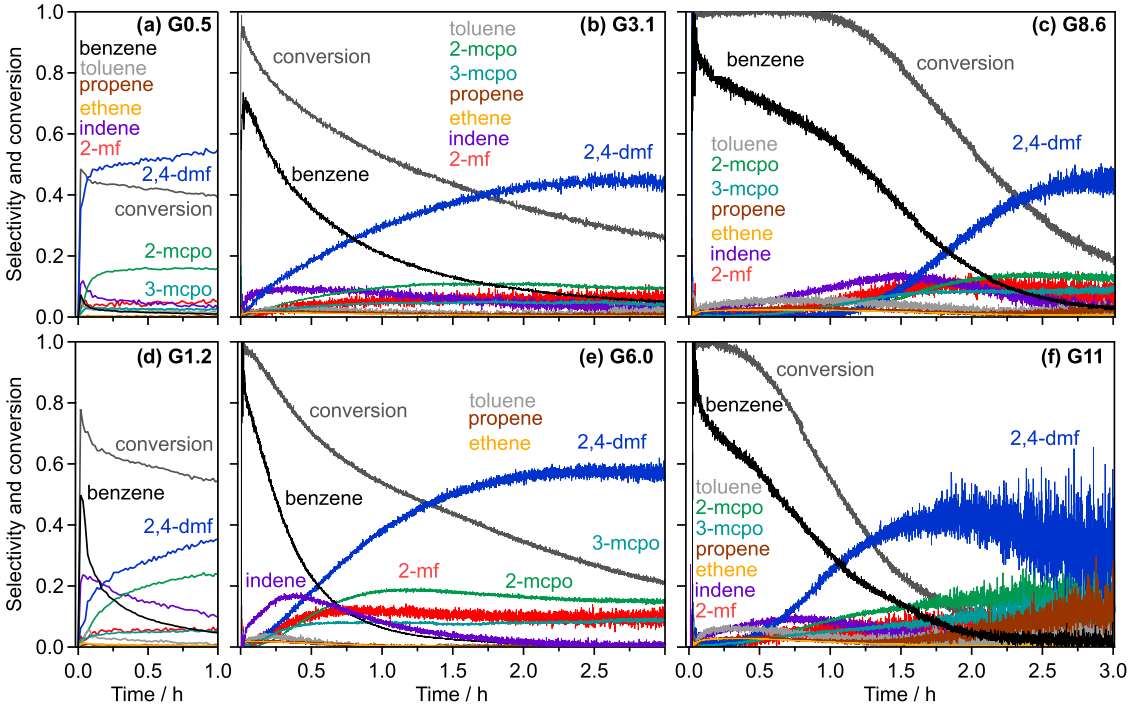

Figure 4. Conversion of 2,5-dmf and selectivities of the main products over zeotypes with a gallium content of 0.5 (a), 1.2 (d), 3.1 (b), 6.0 (e), 8.6 (c), and 11 (f). Concentrations were determined every 2 s (G6.0, G8.6, G11), 4 s (G3.1), or 60 s (G0.5, G1.2) and the reaction was run for 1 h (G0.5, G1.2) or 3 h (other catalysts).

uninhibited production of external coke on the surface and thus quicker deactivation of the catalyst.[1]

Catalyst Deactivation and Mechanistic Insights. To further investigate the regeneration of the catalysts, zeotypes G6.0, G6.7, G8.6, and G11 were subjected to 4 more cycles of 3 h of 2,5-dmf conversion at 500 °C, as shown in Figure S12 in the SI. For each zeotype, the conversion of 2,5-dmf and selectivity toward benzene gradually decrease with each cycle, likely due to the loss of acid sites. To illustrate, after 5 cycles, the zeotypes G6.0, G6.7, G8.6, and G11, possessed roughly 85, 85, 80, and 69% of their initial acid sites, respectively (Table S8 in the SI). Remarkably, G11 showed hardly any reduction in conversion of 2,5-dmf and selectivity to benzene over the course of the 5 cycles, although it experienced the largest decrease in acid sites of 31% after 5 cycles. This indicates that the function of the lost acid sites is taken over by other acid sites, since the acid site density is sufficiently high.

After five cycles, G6.7, G8.6, and G11, were exposed to a sixth cycle (not shown) to allow for the analysis of the spent catalyst using XRD, N_2-physisorption, TGA/DSC, SEM, and EDX, as shown in Table S7 in the SI. The selectivity to coke after 1 cycle appears to increase when the gallium content is increased, ranging from 4.2% for G0.5 to 16.4% for G11 (Table 1). Normalizing to the benzene production, the most benzene per coke molecule is formed in the order of G8.6 > G6.7 > G11. The absolute weight of the coke was determined by TGA between 400 and 900 °C (Figure S13 in the SI), and decreases in the order of G6.7 > G11 > G8.6. This further confirms that different coke species are formed on different zeotypes, and that G6.7 may have experienced faster deactivation than G8.6 due to its smaller crystal size and thus higher external coke formation. Structural analysis of the spent catalysts by XRD revealed that the MFI framework remained intact (Figure S14 in the SI), although coke-induced unit cell distortion has taken place, demonstrated by the transformation of a doublet of diffraction peaks into one at 23.2 2θ, as well as at 45.3 2θ.[60−62]

The morphological features of the coked zeotypes were analyzed by SEM and EDX, shown in Figures S15 and S16 in the SI, respectively. SEM reveals that the coked zeotypes possess a morphology that is similar to their fresh counterparts, though the measured particles were directly taken from the reactor setup and thus in the size range of 300 to 355 μm. EDX analysis (map and point spectra) of G6.7-coked reveals that the main components Si, O, Ga, and C, are all well dispersed over the surface of the catalyst and that the measured coke content is between 7 and 14 wt %. The impurity potassium was not measured and was most likely removed during the reaction or covered by coke.

To determine the correlation between catalyst deactivation and its acidity, NH_3-TPD was performed on the most active catalysts after the reaction (S17 in the SI). The acid site density of all zeotypes decreases substantially during the reaction (black), as is quantified and shown in Table S8 in the SI. In particular, the numbers of strong and extra-strong acid sites are reduced, confirming that the formation of both benzene and coke occurs on these sites.

The regeneration step after the reaction recovered most of the acid sites, ranging from 84% recovered for G11 to 94% for G6.7. The reduction in the number of acid sites is either caused by the migration of gallium under high reaction temperatures, leading to sintering and formation of clusters and nanoparticles, or by the incomplete removal of coke. Although some hard coke species require temperatures beyond 600 °C to be removed, this upper temperature limit was chosen to prevent damaging the catalyst.

Pyridine FTIR adsorption was performed on the coked zeotypes G6.7, G8.6, and G11, after 6 cycles of 3 h conversion

https://doi.org/10.1021/acs.iecr.4c03465
Ind. Eng. Chem. Res. 2025, 64, 2025−2035

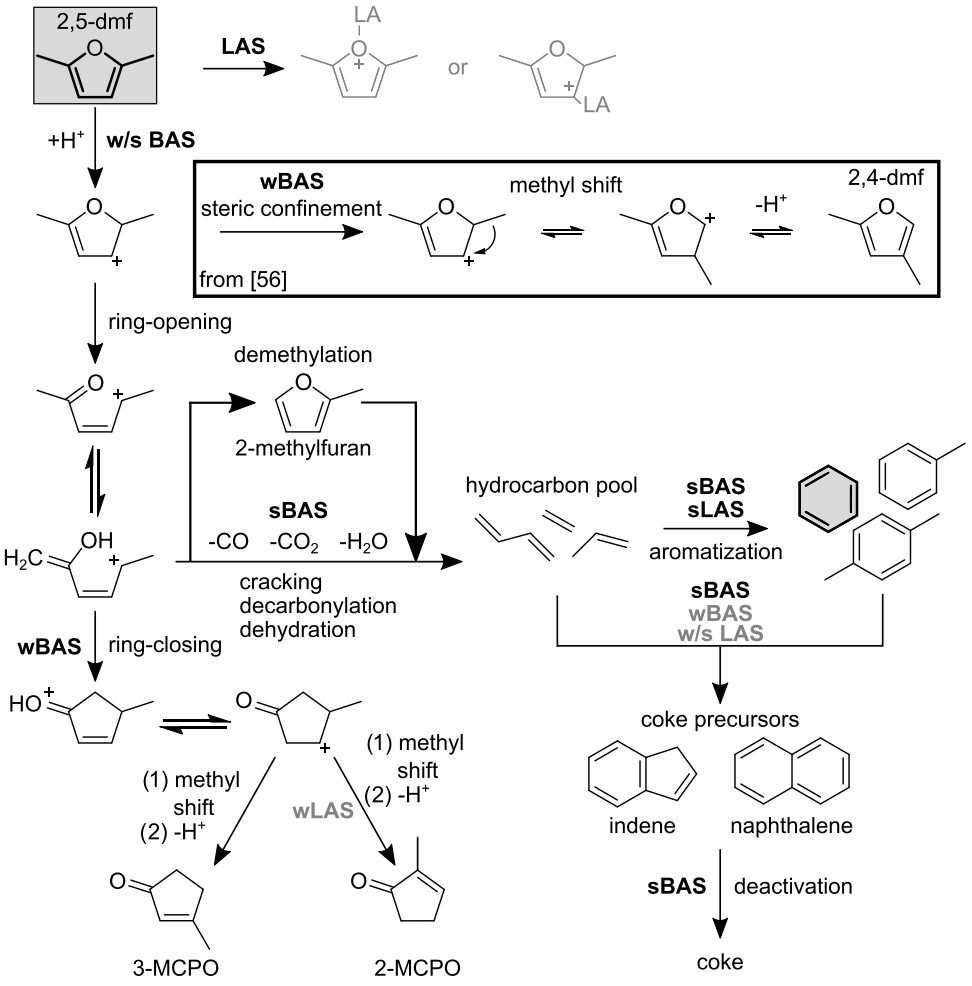

Figure 5. Proposed reaction pathways for the conversion of 2,5-dimethylfuran over Ga-zeotypes at 500 °C.

at 500 °C, as shown in Figure 2. Compared to their fresh counterparts, coked zeotypes have lost most of their strong Brønsted acid sites, with only 14, 12, and 7.8% of sBAS remaining for G6.7, G8.6, and G11, respectively. The number of weak sites was reduced to a lesser extent, indicating that these do not play a major role in the formation of benzene and coke as they are likely not strong enough for cracking, decarbonylation, and dehydration. Instead, their role in the isomerization reactions of 2,5-dmf into 2,4-dmf, 2-mcpo, and 3-mcpo is confirmed, seeing as these are still formed after 3 h TOS.

Interpreting the different conversion behaviors of G6.7 and G8.6 based on their acidity proves to be challenging, owing to their similar acid site distribution and acid site density (0.423 and 0.433 mmol g^{-1}, respectively). However, through analysis of the acid site distribution of the coked zeotypes, the following insights are generated: G6.7 has lost more of its wBAS (76%) than G8.6 (59%), while G8.6 has in turn lost more of its sLAS (69 vs 57% over G6.7). This is in line with the increased production of 2,4-dmf over the wBAS of G6.7, of which some deactivate, as well as with the increased benzene production over 3 h of G8.6, promoted by sLAS. Additionally, the rapid deactivation toward benzene over G11 has been previously assigned to its high number of sBAS, rapidly promoting the formation of benzene and coke. In fact, analysis of the coked zeotype G11c shows that it still possesses 49% of its wBAS, 91% of its wLAS, and 94% of its sLAS after complete deactivation, indicating that the LAS were hardly involved in the reaction or have not had the possibility to participate before sBAS completely coked and G11 deactivated.

This stresses the importance of a balance between the number of strong BAS and strong LAS, as the ratio sBAS/sLAS is 2.2, 2.0, and 4.5 for G6.7, G8.6, and G11, respectively. LAS can promote aromatization to benzene provided that there are sufficient sBAS to initiate the reaction, as has been shown for G6.7 and G8.6 compared to G6.0. However, when there are too many sBAS, rapid coking results in blocking the accessibility to wBAS, wLAS, and sLAS, either by blocking the micropores or encapsulating particles, as was observed for G11. This results in the complete deactivation toward both aromatics and isomers although there is still a high fraction of uncoked wBAS.

Based on the catalytic tests, as well as the analysis of the acidity of the zeotypes, presented in this work, the following reaction scheme is proposed (Figure 5). First, 2,5-dmf binds to either a Lewis acid site (not explored, grayed out) or a Brønsted acid site, resulting in protonation and saturation of one of the double bonds. This intermediate was determined to be more likely to form than *O*-H^+-dimethylfuran.[58] Subsequently, it can be converted over a wBAS in a micropore to 2,4-dmf through a methyl shift.[58] In addition, ring-opening can occur on sBAS resulting in cracking, decarbonylation, and dehydration, into smaller molecules such as ethene, propene, and butadiene; constituting the hydrocarbon pool. This is

https://doi.org/10.1021/acs.iecr.4c03465
Ind. Eng. Chem. Res. 2025, 64, 2025−2035

followed by aromatization into monocyclic aromatics, promoted by sBAS and sLAS, or polycyclic aromatics, promoted by sBAS and potentially wBAS and LAS too. If this preferred mechanistic route is impeded, for example because of the deactivation of sBAS, isomerization dominates through the formation of 2,4-dmf or 2- and 3-mcpo through ring-closing followed by another methyl shift and deprotonation. We hypothesize that deprotonation could also result in the formation of 4-mcpo, although this molecule was not part of the reference database and therefore has not been detected. The conversion of 2-mcpo was favored over 3-mcpo and possibly promoted by wLAS, although 3-mcpo was observed before 2-mcpo over every zeotype; this suggests that 3-mcpo could be an intermediate for 2-mcpo. Further conversion experiments using different feedstocks, such as 2-methylfuran, 2,4-dmf, 2-mcpo, or 3-mcpo, could help elucidate the mechanism.

CONCLUSIONS

Phase-pure gallium zeotypes have been successfully synthesized comprising the MFI framework. High gallium contents can be realized by increasing the duration of the hydrothermal crystallization step or by using TPAOH as template. An increase in gallium content results in a decrease in specific surface area and microporous volume due to the formation of Ga-based nanoparticles, e.g., GaO_x. The gallium content has been shown to play an important role in the conversion of 2,5-dmf into aromatics like benzene. An increase in gallium content results in an increase in the conversion and selectivity toward benzene. However, after 0.5 to 1.5 h, the catalyst deactivates due to the formation of coke and the selectivity toward aromatics and benzene drops rapidly. Instead, the isomerization product 2,4-dmf becomes the main product, accompanied by the isomerization products 2-mcpo and 3-mcpo. Acid site analysis has determined that benzene is mainly formed on the strong and extra-strong Brønsted acid sites, promoted by strong and extra-strong Lewis acid sites, while coke is formed on sBAS which could be promoted by wBAS and LAS. The isomerization products are formed on the weak Brønsted acid sites. Regeneration of the acid sites was possible and the catalysts were active for four more cycles without a major loss of performance.

A gallium content of 6.7 wt % was optimal for a TOS up to 1 h, after which the zeotype with 8.6 wt % Ga produced the most benzene, suggesting that the additional gallium promoted the aromatization toward benzene instead of coke, most likely as sLAS. When the gallium content is too high, i.e., 11 wt %, the high number of sBAS favors rapid formation of coke leading to the deactivation of the catalyst. The importance of a balanced ratio between BAS and LAS, more specifically sBAS and sLAS, is shown, amounting to an optimal ratio of sBAS:sLAS = 2.0

This work explores the conversion of 2,5-dmf into aromatics like benzene, highlights the tunability of Ga-MFI zeotypes, and highlights the importance of the gallium content and acid site distribution for the optimization of this reaction.

Further work could focus on mapping the exact location of gallium in the zeotype, clarifying the character and role of specific gallium species, and elucidating the reaction mechanism by cofeeding reagents or using different feedstocks.

ASSOCIATED CONTENT

Supporting Information

The Supporting Information is available free of charge at https://pubs.acs.org/doi/10.1021/acs.iecr.4c03465.

Detailed description of the catalyst synthesis, experimental methods, structural characterization, catalytic performance tests, and long-term stability tests (PDF)

AUTHOR INFORMATION

Corresponding Authors

Guido J. L. de Reijer − *Department of Chemistry and Chemical Engineering, Chalmers University of Technology, SE-412 96 Gothenburg, Sweden;* orcid.org/0000-0001-7772-7759; Phone: +46 (0)31 772 2907; Email: guidod@chalmers.se

Per-Anders Carlsson − *Department of Chemistry and Chemical Engineering, Chalmers University of Technology, SE-412 96 Gothenburg, Sweden;* orcid.org/0000-0001-6318-7966; Phone: +46 (0)31 772 2924; Email: per-anders.carlsson@chalmers.se

Authors

Andreas Schaefer − *Department of Chemistry and Chemical Engineering, Chalmers University of Technology, SE-412 96 Gothenburg, Sweden;* orcid.org/0000-0001-6578-5046

Anders Hellman − *Department of Physics, Chalmers University of Technology, SE-412 96 Gothenburg, Sweden;* orcid.org/0000-0002-1821-159X

Complete contact information is available at: https://pubs.acs.org/10.1021/acs.iecr.4c03465

Notes

The authors declare no competing financial interest.

ACKNOWLEDGMENTS

The authors thank the Swedish Energy Agency [No. 48569-1] and the Swedish Research Council [No. 2023-06344] for the financial support. Chalmers Materials Analysis Laboratory (CMAL) and the Surface Area and Porosity Laboratory of the Applied Chemistry division are acknowledged for their instrumental support.

REFERENCES

(1) Sun, Y.; Wei, L.; Zhang, Z.; Zhang, H.; Li, Y. Coke Formation over Zeolite Catalysts in Light Alkanes Aromatization and Anti-Carbon-Deposition Strategies and Perspectives: A Review. *Energy Fuels* **2023**, *37*, 1657−1677.

(2) Richardson, J. *Benzene, the Need for A New Global Industrial Revolution and the Big Challenges That Lie Ahead*. https://www.icis.com/asian-chemical-connections/2021/11/30/, 2021; accessed Sept 12, 2024.

(3) Bulushev, D. A.; Ross, J. R. Catalysis for conversion of biomass to fuels via pyrolysis and gasification: A review. *Catal. Today* **2011**, *171*, 1−13.

(4) Bridgwater, A. V. Catalysis in thermal biomass conversion. *Appl. Catal., A* **1994**, *116*, 5−47.

(5) Thring, R. W.; Katikaneni, S. P.; Bakhshi, N. N. Theproduction of gasoline range hydrocarbons from Alcell lignin using HZSM-5 catalyst. *Fuel Process. Technol.* **2000**, *62*, 17−30.

(6) de Jong, E.; Higson, A.; Walsh, P.; Wellisch, M. *Bio-Based Chemicals Value Added Products from Biorefineries*, 2012.

(7) Parikka, M. Global biomass fuel resources. *Biomass Bioenergy* **2004**, *27*, 613−620.

(8) Ragauskas, A. J.; Williams, C. K.; Davison, B. H.; Britovsek, G.; Cairney, J.; Eckert, C. A.; Frederick, W. J.; Hallett, J. P.; Leak, D. J.; Liotta, C. L.; Mielenz, J. R.; Murphy, R.; Templer, R.; Tschaplinski, T. The Path Forward for Biofuels and Biomaterials. *Science* **2006**, *311*, 484−489.
(9) Román-Leshkov, Y.; Barrett, C. J.; Liu, Z. Y.; Dumesic, J. A. Production of dimethylfuran for liquid fuels from biomass-derived carbohydrates. *Nature* **2007**, *447*, 982−985.
(10) Climent, M. J.; Corma, A.; Iborra, S. Conversion of biomass platform molecules into fuel additives and liquid hydrocarbon fuels. *Green Chem.* **2014**, *16*, 516−547.
(11) Rahman, M. M.; Liu, R.; Cai, J. Catalytic fast pyrolysis of biomass over zeolites for high quality bio-oil - A review. *Fuel Process. Technol.* **2018**, *180*, 32−46.
(12) Sheldon, R. A. Green and sustainable manufacture of chemicals from biomass: state of the art. *Green Chem.* **2014**, *16*, 950−963.
(13) Kucherov, F. A.; Romashov, L. V.; Averochkin, G. M.; Ananikov, V. P.; Biobased, C. Biobased C_6-Furans in Organic Synthesis and Industry: Cycloaddition Chemistry as a Key Approach to Aromatic Building Blocks. *ACS Sustainable Chem. Eng.* **2021**, *9*, 3011−3042.
(14) Bielski, R.; Grynkiewicz, G. Furan platform chemicals beyond fuels and plastics. *Green Chem.* **2021**, *23*, 7458−7487.
(15) Gong W, W. *Recent Perspectives in Pyrolysis Research*; Bartoli, M.; Giorcelli, M., Eds.; IntechOpen, 2022.
(16) Al Ghatta, A.; Hallett, J. P. Bioderived furanic compounds as replacements for BTX in chemical intermediate applications. *RSC Sustainability* **2023**, *1*, 698−745.
(17) Brandvold, T. A. Carbohydrate Route to Para-Xylene and Terephthalic Acid. U.S. Patent US2010/0331568A1, 2010.
(18) Cheng, Y. T.; Huber, G. W. Production of targeted aromatics by using Diels-Alder classes of reactions with furans and olefins over ZSM-5. *Green Chem.* **2012**, *14*, 3114−3125.
(19) Williams, C. L.; Chang, C. C.; Do, P.; Nikbin, N.; Caratzoulas, S.; Vlachos, D. G.; Lobo, R. F.; Fan, W.; Dauenhauer, P. J. Cycloaddition of Biomass-Derived Furans for Catalytic Production of Renewable p-Xylene. *ACS Catal.* **2012**, *2*, 935−939.
(20) Uslamin, E. A.; Luna-Murillo, B.; Kosinov, N.; Bruijnincx, P. C.; Pidko, E. A.; Weckhuysen, B. M.; Hensen, E. J. Gallium-promoted HZSM-5 zeolites as efficient catalysts for the aromatization of biomass-derived furans. *Chem. Eng. Sci.* **2019**, *198*, 305−316.
(21) Dutta, S.; Bhat, N. S. Catalytic synthesis of renewable p-xylene from biomass-derived 2,5-dimethylfuran: a mini review. *Biomass Convers. Biorefin.* **2023**, *13*, 541−554.
(22) Olson, D. H.; Haag, W. O.; Lago, R. M. Chemical and Physical Properties of the ZSM-5 Substitutional Series. *J. Catal.* **1980**, *61*, 390−396.
(23) Baertsch, C. D.; Funke, H. H.; Falconer, J. L.; Noble, R. D. Permeation of Aromatic Hydrocarbon Vapors through Silicalite-Zeolite Membranes. *J. Phys. Chem. A* **1996**, *100*, 7676−7679.
(24) Coqueblin, H.; Richard, A.; Uzio, D.; Pinard, L.; Pouilloux, Y.; Epron, F. Effect of the metal promoter on the performances of H-ZSM5 in ethylene aromatization. *Catal. Today* **2017**, *289*, 62−69.
(25) Zheng, Y.; Wang, F.; Yang, X.; Huang, Y.; Liu, C.; Zheng, Z.; Gu, J. Study on aromatics production via the catalytic pyrolysis vapor upgrading of biomass using metal-loaded modified H-ZSM-5. *J. Anal. Appl. Pyrolysis* **2017**, *126*, 169−179.
(26) Lok, C.; Van Doorn, J.; Aranda Almansa, G. Promoted ZSM-5 catalysts for the production of bio-aromatics, a review. *Renewable Sustainable Energy Rev.* **2019**, *113*, No. 109248.
(27) Espindola, J. S.; Gilbert, C. J.; Perez-Lopez, O. W.; Trierweiler, J. O.; Huber, G. W. Conversion of furan over gallium and zinc promoted ZSM-5: The effect of metal and acid sites. *Fuel Process. Technol.* **2020**, *201*, No. 106319.
(28) Li, J.; Li, X.; Hua, D.; Lu, X.; Wang, Y. Optimizing the aromatic product distribution from catalytic fast pyrolysis of biomass using hydrothermally synthesized Ga-MFI zeolites. *Catalysts* **2019**, *9*, 854.
(29) Xin, M.; Xing, E.; Gao, X.; Wang, Y.; Ouyang, Y.; Xu, G.; Luo, Y.; Shu, X. Ga Substitution during Modification of ZSM-5 and Its Influences on Catalytic Aromatization Performance. *Ind. Eng. Chem. Res.* **2019**, *58*, 6970−6981.
(30) Sauer, C.; de Reijer, G. J. L.; Schaefer, A.; Carlsson, P.-A. Isomorphous Substitution of Gallium into MFI-Framework Zeolite Increases 2,5-Dimethylfuran to Aromatics Selectivity and Suppresses Catalyst Deactivation. *Top. Catal.* **2023**, *66*, 1329−1340.
(31) Miyamoto, T.; Katada, N.; Kim, J. H.; Niwa, M. Acidic property of MFI-type gallosilicate determined by temperature-programmed desorption of ammonia. *J. Phys. Chem. B* **1998**, *102*, 6738−6745.
(32) Fang, Y.; Su, X.; Bai, X.; Wu, W.; Wang, G.; Xiao, L.; Yu, A. Aromatization over nanosized Ga-containing ZSM-5 zeolites prepared by different methods: Effect of acidity of active Ga species on the catalytic performance. *J. Energy Chem.* **2017**, *26*, 768−775.
(33) Creci, S.; Martinelli, A.; Vavra, S.; Carlsson, P.-A.; Skoglundh, M. Acidity as descriptor for methanol desorption in B-, Ga-and Ti-MFI zeotypes. *Catalysts* **2021**, *11*, No. 97.
(34) Creci, S.; Wang, X.; Carlsson, P.-A.; Skoglundh, M. Tuned Acidity for Catalytic Reactions: Synthesis and Characterization of Fe- and Al-MFI Zeotypes. *Top. Catal.* **2019**, *62*, 689−698.
(35) Brunauer, S.; Emmett, P. H.; Teller, E. Adsorption of Gases in Multimolecular Layers. *J. Am. Chem. Soc.* **1938**, *60*, 309−319.
(36) Rouquerol, J.; Llewellyn, P.; Rouquerol, F. Is the BET equation applicable to microporous adsorbents? *Stud. Surf. Sci. Catal.* **2007**, *160*, 49−56.
(37) Jura, G.; Harkins, W. D. Surfaces of Solids. XI. Determination of the Decrease (π) of Free Surface Energy of a Solid by an Adsorbed Film. *J. Am. Chem. Soc.* **1944**, *66*, 1356−1362.
(38) Galarneau, A.; Villemot, F.; Rodriguez, J.; Fajula, F.; Coasne, B. Validity of the t-plot method to assess microporosity in hierarchical micro/mesoporous materials. *Langmuir* **2014**, *30*, 13266−13274.
(39) Sauer, C.; Lorén, A.; Schaefer, A.; Carlsson, P.-A. On-Line Composition Analysis of Complex Hydrocarbon Streams by Time-Resolved Fourier Transform Infrared Spectroscopy and Ion−Molecule Reaction Mass Spectrometry. *Anal. Chem.* **2021**, *93*, 13187−13195.
(40) Sauer, C.; Lorén, A.; Schaefer, A.; Carlsson, P.-A. Valorisation of 2,5-dimethylfuran over zeolite catalysts studied by on-line FTIR-MS gas phase analysis. *Catal.:Sci. Technol.* **2022**, *12*, 750−761.
(41) Inui, M.; Ikeda, T.; Suzuki, T.; Sugita, K.; Mizukamil, F. Quantitative Analysis of Structural Defect in Silicalite by Rietveld Refinements using X-ray Powder Diffraction and ^{29}Si MAS NMR. *Bull. Chem. Soc. Jpn.* **2009**, *82*, 1160−1169.
(42) Ungár, T. Microstructural parameters from X-ray diffraction peak broadening. *Scr. Mater.* **2004**, *51*, 777−781.
(43) Kosslick, H.; Tuan, V. A.; Parlitz, B.; Fricke, R.; Peuker, C.; Storek, W. Disruption of the MFI framework by the incorporation of gallium. *J. Chem. Soc., Faraday Trans.* **1993**, *89*, 1131−1138.
(44) Kihara, K. An X-ray study of the temperature dependence of the quartz structure. *Eur. J. Mineral.* **1990**, *2*, 63−78.
(45) Fleet, M. E. Structures of low gallium albite ($NaGaSi3_3O_8$) and intermediate germanium albite ($NaAlGe_3O_8$): tetrahedral-site ordering in sodium feldspar. *Am. Mineral.* **1991**, *76*, 92−99.
(46) Thommes, M.; Kaneko, K.; Neimark, A. V.; Olivier, J. P.; Rodriguez-Reinoso, F.; Rouquerol, J.; Sing, K. S. Physisorption of gases, with special reference to the evaluation of surface area and pore size distribution (IUPAC Technical Report). *Pure Appl. Chem.* **2015**, *87*, 1051−1069.
(47) Groen, J. C.; Peffer, L. A.; Pérez-Ramírez, J. Pore size determination in modified micro- and mesoporous materials. Pitfalls and limitations in gas adsorption data analysis. *Microporous Mesoporous Mater.* **2003**, *60*, 1−17.
(48) De Lange, M. F.; Vlugt, T. J.; Gascon, J.; Kapteijn, F. Adsorptive characterization of porous solids: Error analysis guides the way. *Microporous Mesoporous Mater.* **2014**, *200*, 199−215.
(49) Silvestre-Albero, A. M.; Juárez-Galán, J. M.; Silvestre-Albero, J.; Rodríguez-Reinoso, F. Low-pressure hysteresis in adsorption: An artifact? *J. Phys. Chem. C* **2012**, *116*, 16652−16655.
(50) Müller, U.; Unger, K. K. Sorption studies on large ZSM-5 crystals: The influence of aluminium content, the type of

https://doi.org/10.1021/acs.iecr.4c03465
Ind. Eng. Chem. Res. 2025, 64, 2025−2035

exchangeable cations and the temperature on nitrogen hysteresis effects. *Stud. Surf. Sci. Catal.* **1988**, *39*, 101−108.
(51) Müller, U.; Reichert, H.; Robens, E.; Unger, K. K.; Grillet, Y.; Rouquerol, F.; Rouquerol, J.; Pan, D.; Mersmann, A. High-resolution sorption studies of argon and nitrogen on large crystals of microporous zeolite ZSM-5. *Fresenius' Z. Anal. Chem.* **1989**, *333*, 433−436.
(52) Rouquerol, F.; Rouquerol, J.; Sing, K.; Llewellyn, P.; Maurin, G. *Academic Press*; Academic Press, 2014; pp 505−506.
(53) Reichert, H.; Müller, U.; Unger, K. K.; Grillet, Y.; Rouquerol, F.; Rouquerol, J.; Coulomb, J. P. Sorption of argon and nitrogen on network types of zeolites and aluminophosphates. *Stud. Surf. Sci. Catal.* **1991**, *62*, 535−542.
(54) Llewellyn, P. L.; Coulomb, J. P.; Grillet, Y.; Patarin, J.; Lauter, H.; Reichert, H.; Rouquerol, J. Adsorption by MFI-Type Zeolites Examined by Isothermal Microcalorimetry and Neutron Diffraction. 1. Argon, Krypton, and Methane. *Langmuir* **1993**, *9*, 1846−1851.
(55) Parry, E. P. An Infrared Study of Pyridine Adsorbed on Acidic Solids. Characterization of Surface Acidity. *J. Catal.* **1963**, *2*, 371−379.
(56) Emeis, C. A. Determination of integrated molar extinction coefficients for infrared absorption bands of pyridine adsorbed on solid acid catalysts. *J. Catal.* **1993**, *141*, 347−354.
(57) Ravi, M.; Sushkevich, V. L.; van Bokhoven, J. A. Towards a better understanding of Lewis acidic aluminium in zeolites. *Nat. Mater.* **2020**, *19*, 1047−1056.
(58) Sauer, C.; de Reijer, G. J. L.; Wilfinger, B.; Hellman, A.; Carlsson, P.-A. Continuous isomerisation of 2,5-dimethylfuran to 2,4-dimethylfuran over Ga-silicate. *Chem. - Eur. J.* **2024**, *30*, No. e202303810.
(59) Wang, C.; Hu, M.; Chu, Y.; Zhou, X.; Wang, Q.; Qi, G.; Li, S.; Xu, J.; Deng, F. π-Interactions between Cyclic Carbocations and Aromatics Cause Zeolite Deactivation in Methanol-to-Hydrocarbon Conversion. *Angew. Chem., Int. Ed.* **2020**, *59*, 7198−7202.
(60) Alvarez, A. G.; Viturro, H.; Bonetto, R. D. Structural changes on deactivation of ZSM-5. A study by X-ray powder diffraction. *Mater. Chem. Phys.* **1992**, *32*, 135−140.
(61) Rojo-Gama, D.; Nielsen, M.; Wragg, D. S.; Dyballa, M.; Holzinger, J.; Falsig, H.; Lundegaard, L. F.; Beato, P.; Brogaard, R. Y.; Lillerud, K. P.; Olsbye, U.; Svelle, S. A Straightforward Descriptor for the Deactivation of Zeolite Catalyst H-ZSM-5. *ACS Catal.* **2017**, *7*, 8235−8246.
(62) Rojo-Gama, D.; Mentel, L.; Kalantzopoulos, G. N.; Pappas, D. K.; Dovgaliuk, I.; Olsbye, U.; Lillerud, K. P.; Beato, P.; Lundegaard, L. F.; Wragg, D. S.; Svelle, S. Deactivation of Zeolite Catalyst H-ZSM-5 during Conversion of Methanol to Gasoline: Operando Time- and Space-Resolved X-ray Diffraction. *J. Phys. Chem. Lett.* **2018**, *9*, 1324−1328.

https://doi.org/10.1021/acs.iecr.4c03465
Ind. Eng. Chem. Res. 2025, 64, 2025−2035